Quasiparticle self-consistent *GW* band structure of CrN

Tawinan Cheiwchanchamnangij

Department of Physics, Faculty of Science, Mahidol University, Bangkok 10400, Thailand

Walter R. L. Lambrecht ●

Department of Physics, Case Western Reserve University, 10900 Euclid Avenue, Cleveland, Ohio 44106-7079, USA

The band structures of CrN are calculated using the quasiparticle self-consistent *GW* approach in both the low-temperature antiferromagnetic (AFM) $[110]_2$ *Pmna* orthorhombic phase and in a hypothetical ferromagnetic phase representing the paramagnetic cubic state in a saturating magnetic field. A gap of about 1 eV is found in the AFM state, while the ferromagnetic band structure is found to be half metallic. Another hypothetical AFM-1 structure $[001]_1$ is also considered and gives a smaller band gap. The orbital nature of the bands is studied and reveals a gap between Cr-*d* states, indicating a strongly correlated behavior. Optical dielectric functions are calculated from the interband transitions and compared to experimental data.

I. INTRODUCTION

Transition metal nitrides, such as CrN, have interesting magnetic behavior and possibly correlated electronic structure resulting from the partially filled *d* bands. CrN in particular is known to exhibit an antiferromagnetic state, accompanied by a slight structural distortion below 273–286 K [1]. The ordering corresponds to $[110]_2$ meaning that in the [110] direction the spins order in ferromagnetic planes with alternating, two spin up planes, and two spin down. The resulting structure is orthorhombic with space group *Pmna*. We will also refer to it as the AFM-2 phase, while an alternative hypothetical antiferromagnetic (AFM) ordering $[001]_1$ will be called AFM-1.

While the magnetic properties of the AFM-2 phase are fairly well understood, the optical and transport properties and the underlying electronic band structure have been rather controversial and have received a significant attention since about 2000. As pointed out by Herwadkar and Lambrecht [2] and more fully documented there, resistivities ranging over 6 orders of magnitude have been reported for CrN. While no doubt this reflects mostly the difficulty in obtaining stoichiometric CrN and points to an important role for defects, such as N vacancies, the nature of the electronic band structure, metallic or semiconducting, is still not fully resolved. According to the pioneering work by Corliss *et al.* [1] the system is metallic both above and below the Néel transition temperature T_N. Similar behavior is reported by Wang *et al.* [3] although their transition temperature is significantly lower. Herle *et al.* [4] found semiconducting behavior with a gap of 0.09 eV on powders. Quintela *et al.* [5] found semiconducting behavior in the paramagnetic phase with an activation energy of 75 meV but concluded that in the AFM phase the behavior was neither conventional semiconducting nor fully itinerant although hole doping in $Cr_{1-x}V_xN$ drives it to itinerant behavior. Anderson *et al.* [6] studied $In_{1-x}Cr_xN$ and found semi-

conducting behavior with an indirect gap of about 0.7 eV for AFM CrN both based on resistivity and on optical reflectivity and transmission. Constantin *et al.* [7] surprisingly found semiconducting behavior above the transition temperature but metallic behavior below T_N for CrN grown epitaxially on MgO (001) by molecular-beam epitaxy. Meanwhile, Gall *et al.* [8], also growing CrN on MgO (but by magneton sputtering), found an increasing conductivity with increasing temperature over the whole temperature range suggesting semiconducting behavior without any sign of the phase transition and reported an optical gap of 0.7 eV. They suggested the possibility that CrN would be a Mott insulator.

In terms of transport, the group of Gall *et al.* found a variable range hoppinglike conductivity [8,9]. Later on, this group showed convincingly that the epitaxial constraint on MgO can suppress the phase transition while in polycrystalline samples, grown under identical conditions but on a nonmatching substrate quartz, the phase transition was present [10]. The conductivity in polycrystalline samples was found to be two to three orders of magnitude larger than that in epitaxially constrained samples, and much less dependent on temperature, suggesting metallic behavior. They also show that a drop in conductivity occurs at the phase transition. Below T_N the conductivity was found to be decreasing (increasing) with decreasing temperature in samples grown at 600 (800) °C. They explained the decreasing conductivity with decreasing temperature below the transition temperature in terms of strong disorder rather than the presence of a gap. In the paramagnetic cubic phase above the transition temperature, which persists down to low temperatures if the transition is epitaxially suppressed, they found a gap and semiconducting behavior although with variable range hopping. The metallic behavior found in some other works in this paramagnetic phase is then ascribed to high doping by for example N vacancies. They also showed that the behavior of the conductivity with temperature is strongly dependent on

growth temperature. Other growth conditions, such as angle of deposition, were also found to strongly affect the CrN morphology [11,12].

The overall conclusion emerging from the extensive work of Gall's group is that the paramagnetic phase is insulating while the the AFM $[110]_2$ phase in polycrystalline films was found to be metallic. In contrast the cubic phase could be stabilized down to low temperatures by epitaxy and then remains insulating although not with a conventional activated semiconducting behavior but rather a variable range hopping. Metallic character in the AFM phase was confirmed by photoemission studies by Bhobe *et al.* [13]. In particular, while both above and below T_N they see no evidence of a finite DOS at the VBM using high-energy x-ray resonant Cr $2p - 3d$ photoemission but with high resolution laser source photoemission, they see a clear Fermi edge. This is done with a low-energy 6.9-eV photon source which has a penetration depth of about 100 Å. In spite of the intensive studies, the conduction mechanism below T_N is still not clear and indications of insulating behavior are clearly present in the work of Quintela *et al.* [5] and Anderson *et al.* [6].

After Gall *et al.*'s [8] initial suggestion of a Mott-insulating behavior, Herwadkar and Lambrecht [2] used the LSDA+U method to investigate this possibility computationally. While various methods were used to estimate U, the results were not entirely unambiguous. They suggested a gap could open due to preferential filling of the Cr $t_{2g} \uparrow$ states. However, to open this gap in a ferromagnetic state required a rather large $U > 5$ eV. With a more realistic value of U, of about 3 eV, a gap already opens in the AFM state, in particular in the AFM$[110]_2$ phase. Nonetheless, this gap was rather small, and it was concluded that the optical gap seen by Gall *et al.* [8] corresponded to the smallest direct gap transitions but a much smaller indirect gap (of order 0.1 eV or lower) would exist and would determine the transport behavior. This was confirmed by an extensive study of the optical properties by Zhang and Gall [14] who found a strong absorption onset at about 0.64 eV and matched higher lying peaks in ε_2 tentatively to other band features reported in Ref. [2]. Optical studies were also reported by Ebad-Allah *et al.* [15] and confirm the results of Zhang and Gall but extend them by studying the temperature and pressure dependence.

Bhobe *et al.* [13] determined the Hubbard U value experimentally by using the LVV Auger transition and arrived at a value of $U \approx 4.5$ eV. Their careful comparison of the valence-band photoemission also confirms the picture of a strongly correlated system with a sizable U. Nonetheless, there remains a difficulty to explain discrepancy between theory and experiment, because LSDA+U theory predicts the largest gap for the AFM $[110]_2$ phase, rather than for the ferromagnetic or $[100]_1$ antiferromagnetic phases, while at least some experiments indicate metallic behavior or much lower gap below T_N.

In fact, the study of Herwadkar and Lambrecht [2] leaves considerable uncertainty for the nature of paramagnetic phase. Modeling the paramagnetic phase above T_N in LSDA+U is not trivial because one should not just do non-spin-polarized calculations but in fact treat the disorder of the spin directions. That problem was addressed by Alling *et al.* [16]. They used a special quasirandom structure (SQS) model to simulate

the randomness of the magnetic moments, which in spite of still being a collinear spin model, captures some of the essence of the paramagnetic state. These authors adjusted their $U \approx 3$ eV value to reproduce as well as possible the lattice constant of the cubic NaCl phase as well as the distortion in the AFM$[110]_2$ phase. Their calculation of the density of states (DOS) confirms that there is definitely a gap in the paramagnetic phase even with a relatively small U value. The focus of this group however was on the structural properties. A similar approach to modeling paramagnetic phases by means of SQS supercells has recently been used by Trimarchi *et al.* [17] for various transition metal oxides and by Varignon *et al.* [18,19] for perovskites. Besides these questions of the band gap, another controversy emerged over CrN, namely the reported strong reduction or even "collapse" of the bulk modulus under pressure, reported by Rivadulla *et al.* [20]. While this softening of the bulk modulus under a pressure induced transition was later invalidated [3], their work and subsequent work by Ebad-Allah *et al.* [15] does show the presence of a magnetoelastic transition under pressure. The coupling of the magnetic ordering to elastic distortion was already well explained by Filipetti *et al.* [21,22]. Steneteg *et al.* [23], using LSDA+U calculations including randomness in the paramagnetic state, also found only a small reduction in bulk modulus under the cubic to orthorhombic phase transition. The vibrational properties and contributions to the free energy were evaluated by Shulumba *et al.* [24] and later by Zhou *et al.* [25]. The other main advantage of the SQS model was that it allowed a study of the exchange interactions in the paramagnetic state [26].

Returning to the gap question, theory and agreement now agree clearly on the existence of a band gap in the paramagnetic phase but there is as yet no consensus on the transport behavior in the antiferromagnetic orthorhombic $[110]_2$ phase. There are several experimental indications that defects and stoichiometry play a key role. The AFM transition temperature also depends on these factors [3,27], and in some cases is completely suppressed [9]. Botana *et al.* [28] studied CrN using various exchange correlation functionals, including hybrid functionals and the Tran-Blaha modified Becke-Johnson (TBmBJ) functional as well as LSDA+U. The TBmBJ functional is well known to increase gaps in many semiconductors. They obtain clearly a gap in the AFM $[110]_2$ phase and confirm the results of Herwadkar *et al.* [2] that a gap is easiest to open (meaning it requires a lower U value) in the orthorhombic AFM phase, compared to other hypothetical phases, such as AFM $[001]_1$ or the ferromagnetic phase. Subsequently, Botana *et al.* [29] ascribed the metallic conductivity below T_N found in some of the studies as possibly being due to the presence of surface states. Meanwhile, it is also clear that N vacancies play an important role in CrN properties. The vacancies were studied by Zhang *et al.* [30] and Mozafari *et al.* [31]. These authors also show that the presence of defects and thermal fluctuations significantly smear the band gap at high temperature and may in fact wipe out the gap. More recently, Rojas and Ulloa studied strain effects and point defects in CrN [32,33].

In the present paper, we reexamine the question of the gap in CrN by means of quasiparticle self-consistent (QS)GW calculations [34,35]. This method has the advantage to be

parameter free and, in principle, is independent of the density functional theory starting point. Nonetheless, we here start from the LSDA+U model which opens a gap, and subsequently remove the U but let the GW self-energy Σ take over its role in opening up the band gap. We study the band structure in both the antiferromagnetic $[110]_2$ *Pmna* orthorhombic phase and the cubic NaCl structure ferromagnetic phase, which might occur at high temperature in a saturating magnetic field aligning the random spins of the paramagnetic phase. We also consider the alternative $[001]_1$ antiferromagnetic phase and find it to have a somewhat lower band gap.

II. COMPUTATIONAL METHOD

The starting point of our calculations is density functional theory (DFT) [36,37] in the local-density approximation (LDA) [38]. This method is used to relax the structure and to obtain the initial band structure. Subsequently, the QS*GW* method is used to calculate the self-energy band shifts. Both are implemented using the full-potential linearized muffin-tin-orbital (FP-LMTO) band-structure method [39,40]. In this method, the basis functions are atom-centered smoothed Hankel functions [41] specified by an inverse decay length κ and a smoothing radius R_{sm} in their radial function and multiplying a spherical harmonic. These are expanded around other sites in spherical harmonic components, using structure constants, and are augmented in all muffin-tin spheres, i.e., matched in value and slope, to a solution $[\phi_{\nu\mathbf{R}l}(r_\mathbf{R})]$ of the Schrödinger equation of the spherical part of the potential at that site $\mathbf{R}$ at some linearization energy ϵ_ν and its energy derivative $[\dot\phi_{\nu\mathbf{R}l}(r_\mathbf{R})]$. This expansion is typically carried out up to a higher angular momentum cutoff ℓ_{maxa} than the cutoff used for the basis set. In the present calculations, we use a double basis set *spdf*-*spd* and use $\ell_{\text{maxa}} = 4$. In addition, we use local orbitals for the Cr-3p states. These are semicore states and are represented by an orbital confined to its muffin-tin sphere with a fixed logarithmic derivative. We stress that the actual potential in the FP-LMTO method does not need to be of muffin-tin form but can have nonspherical components in the spheres and is not constant in the interstitial region but is there represented by the values on a real-space mesh. All quantities are represented in a threefold way in terms of the smooth part represented on the real-space mesh, its expansion in spheres in spherical harmonics, and the actual quantities inside the spheres. The integrals of the Hamiltonian, overlap matrix, charge density, etc., are evaluated as a sum over the mesh minus the integral over the sphere of the smooth spherical expansions in the sphere, which are replaced by the integrals over the sphere of the actual quantities in the sphere. This procedure is, in fact, similar to the one used in the projector-augmented-wave (PAW) method [42], with the difference that instead of projector functions inside the spheres we have the actual augmentation functions, and the actual all-electron core charge densities which are also relaxed at each iteration. The method also allows for calculation of the forces using a force theorem and this can be used to relax the atomic positions in the cell. While we here used experimental lattice constants, the atomic positions were fully relaxed in the structures where they are not fully determined by symmetry.

To start the QS*GW* calculations with already a gapped band structure, we here use the LSDA+U method [43,44] with a $U = 0.294$ eV, $J = 0.069$ value. The initial band structure determines the Green's function G and the polarization function Π^0 used to screen the screened Coulomb interaction $W = (1 - v\Pi^0)^{-1}v = \varepsilon^{-1}v$ from which the self-energy $\Sigma = iGW$ is calculated [45,46]. Note that these are only schematic equations, which represent the actual operator equations. The two-particle operators are expanded in an auxiliary basis set of products of LMTOs combined with interstitial plane waves. From the initial self-energy matrix in the basis of LDA($+U$) eigenstates, one then extracts a new energy-independent but nonlocal exchange correlation potential,

$$\left[v_{xc}^{\Sigma}\right]_{nm} = \tfrac{1}{2}\text{Re}[\Sigma_{nm}(E_n) + \Sigma_{nm}(E_m)]. \tag{1}$$

The bands are then redetermined self-consistently in the presence of this added exchange correlation potential and form the start for the next iteration. At the end of the procedure the Kohn-Sham equation eigenvalues equal the quasiparticle excitation energies. The atom-centered basis set allows us to represent the GW self-energy or its energy-independent average, v_{xc}^{Σ}, in a real-space basis set. This allows then for an efficient interpolation to a finer **k**-point mesh than the one for which the Σ is evaluated by the GW method. This is equivalent, in some sense, to the interpolation by means of Wannier functions, and allows us to obtain the full band structure along symmetry lines, accurate effective masses, etc. To make this interpolation work, it is necessary that the basis set is sufficiently well localized. Therefore slightly more localized basis function κ's are chosen for the GW calculations and also the high-energy part of the Σ matrix is replaced by a diagonal average [35]. In practice, this approximation is here used above a cutoff of 3.5 Ry. The interstitial plane wave cutoff in the auxiliary basis set is set to 2.7 Ry. The GW **k**-point meshes are $8 \times 8 \times 8$ for the ferromagnetic (FM) phase, $6 \times 6 \times 5$ for the AFM-1 phase, and $3 \times 5 \times 7$ for AFM-2 phase while for the self-consistent charge density iterations within the LMTO method the larger meshes of $15 \times 15 \times 15$ for the FM phase, $10 \times 10 \times 8$ for the AFM[001]-1 phase, and $7 \times 10 \times 14$ for the AFM-2 phase are used. The optical dielectric functions use an even finer mesh of $30 \times 30 \times 30$ for the FM phase, $24 \times 24 \times 20$ for the AFM-1 phase, and $9 \times 15 \times 21$ for the AFM-2 phase. Besides the pure QS*GW* results, we also consider the 0.8Σ approach, in which $\Delta\Sigma = \Sigma - v_{xc}^{\text{LDA}}$ is multiplied by a factor 0.8 to simulate the effects of electron-hole coupling in increasing the screening [47,48]. The code for the QS*GW* approach is available as part of the QUESTAAL package [49] and is also available at [50]. The methodology is described comprehensively in Ref. [51].

III. RESULTS

Because the band structure of the cubic NaCl structure is easier to interpret we start with the energy bands of the ferromagnetic state (FM) obtained within the QS*GW* method. We note that, although a ferromagnetic state is not known for CrN, we may think of this as the paramagnetic high-temperature cubic phase in a saturating magnetic field, aligning the magnetic moments.
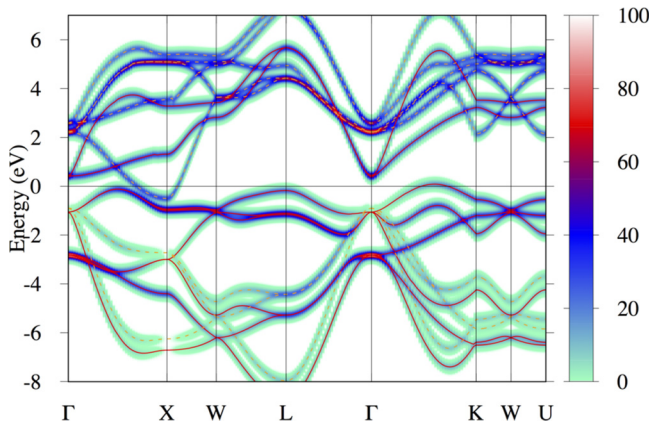
FIG. 1. Energy bands in FM CrN, highlighting the Cr-d contribution. The solid red lines show the majority-spin bands, while the dashed yellow lines show the minority-spin bands. The blue and dark red broad lines show the Cr-d contribution of the band according to the color intensity scale on the right.

FIG. 2. Label of symmetry points on orthorhombic Brillouin zone.

The band structure for the FM case is shown in Fig. 1. The figure highlights the Cr-d contribution and distinguishes up and down spin. We can see that this band structure is qualitatively quite similar to the LSDA+U results of Ref. [2]. Specifically, we note that the strongly d-character band emanating from Γ along Γ-X at about -3 eV, is the $d-t_{2g\uparrow}$ majority-spin band. As already pointed out by Herwadkar and Lambrecht [2], because Cr^{+3} has a configuration of d^3, there is an energetic advantage in preferentially filling the (at Γ) threefold degenerate $t_{2g\uparrow}$ bands. So, this is an orbital polarization as well as spin-polarization effect. Thus one could say that the Hubbard-U, here represented by the QSGW self-energy Σ, pushes these levels down relative to the minority-spin bands of the same orbital character. The higher filled majority-spin bands at Γ have in fact more N-$2p$ character but become more Cr-d like near the valence-band maximum (VBM) along Γ-X. The actual or highest VBM in fact is found along Γ-K and is more N-$2p$-like there, while a Cr-d-like band is running flat at about 1 eV below the VBM. This is one of the $d-t_{2g\uparrow}$ bands while the other two disperse downward away from Γ. The minority-spin d bands in the conduction band of $t_{2g\downarrow}$ character lie at about 2 eV at Γ but one of these bands, the d_{xy} if we are along the [001] direction, is well known in the NaCl structure to disperse downward, while d_{xz}, d_{yz} staying doubly degenerate along Γ-X disperse upward. The downward dispersing d_{xy} band is the minority-spin band which crosses the Fermi level along Γ-X. Further information on the fully m-resolved orbital decomposed bands is given in the Supplemental Material [52]. In fact, this band structure is metallic, or, more specifically, half metallic, with a gap in the majority-spin bands but a band crossing the Fermi level of minority spin. The lowest direct gap between majority-spin states occurs at about 0.4 Γ-X and is 0.90 eV while the direct gap at Γ is 1.47 eV. The VBM of the majority-spin states occurs at 0.6 Γ-K and gives an indirect majority-spin gap of 0.33 eV. Meanwhile, the conduction-band minimum in the majority-spin channel at Γ is the Cr-$d-e_{g\uparrow}$ band and its minority-spin counterpart is seen to lie highest at Γ above the $t_{2g\downarrow}$. We note that in Ref. [2] the $d_{xy\downarrow}$ band barely dips below
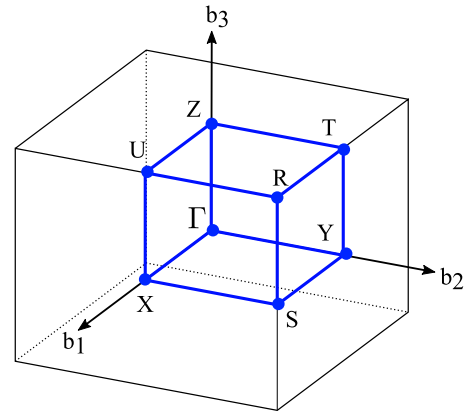
the Fermi level at X, while here it dips about 0.5 eV below it giving a clear half-metallic signature. Since that LSDA+U calculation corresponded to $U = 5$ eV and clearly pushes up this band more than in our QSGW calculation, we may conclude that the QSGW method indicates $U < 5$ eV would be more appropriate.

Next, having understood the FM band structure, we move on to the orthorhombic AFM [110]$_2$ band structure. The Brillouin-zone high-symmetry point labeling used is shown in Fig. 2. We note that the b_1 direction (Γ-X) here corresponds to the cubic [110] direction along which the ferromagnetic layers alter up and down spin every two layers. So, this is the long direction in the real-space unit cell and the shorter one in the Brillouin zone. The [1$\bar{1}$0] cubic direction corresponds to Γ-Y while the [001] cubic direction corresponds to Γ-Z. Because of the 45° rotation of the reciprocal-lattice vectors from the cubic axes, the Γ-X here corresponds to Γ-K in the cubic fcc Brillouin zone. The quadrupling of the cell along this direction (with spins $\uparrow\uparrow\downarrow\downarrow$ per layer) means the band are folded in four along this direction. Hence the multiple degeneracies at X and Γ and S. Despite this somewhat complicated folding of the bands, one may still recognize some relations between the bands in the FM and AFM Brillouin zones.

The band structure of the antiferromagnetic orthorhombic structure is shown in Fig. 3 again highlighting the Cr-d
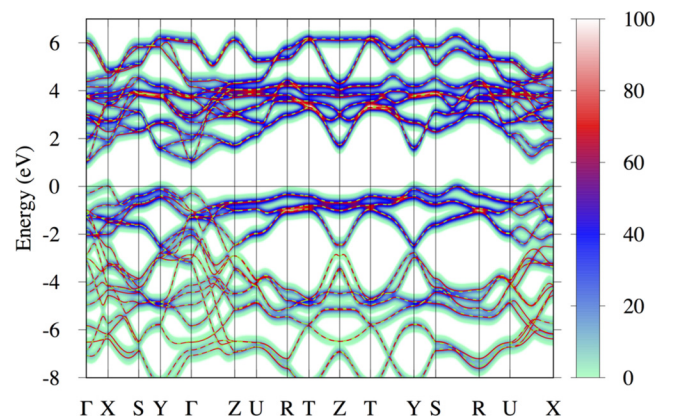

FIG. 3. Band structure of AFM [110]$_2$ CrN with color shading representing the Cr-d contribution.

TABLE I. Calculated magnetic moments m, band gaps, and total-energy differences of various CrN phases. For the FM case, the gap means the majority-spin gap.

	FM	AFM-1	AFM-2
m (μ_B)	2.99	2.71	2.82
E_g^{dir} (eV) QSGW	0.90	0.35	1.34
E_g^{dir} (eV) 0.8Σ	0.47	no gap	0.98
E_g^{indir} (eV) QSGW	0.33	0.24	1.04
E_g^{indir} (eV) 0.8Σ	-0.10	no gap	0.68
ΔE_{tot} (meV/f.u.)	282	79	0

character. The most striking aspect of this band structure is that there is a clear gap of about 1 eV. A strong Cr-d character is seen throughout the upper VBM and about 1 eV below it. The actual VBM occurs at X. The conduction-band minimum (CBM) occurs at Γ and leads to an indirect gap of 1.04 eV, while the direct gap at Γ is 1.34 eV. The CBM also has Cr-d character. The Cr-d character in some bands near -5 eV shows evidence of Cr-N bonding and is related to the Cr-d t_{2g} states also found in the FM case.

Figure 4 shows clearly that the states near the gap are both predominantly Cr-d of the same spin on the same atom. Of course, because of the antiferromagnetic arrangement, a similar DOS occurs with the spins reversed on the other spin Cr atoms. Comparison is also made with the FM and AFM-1 case. It confirms that the minority-spin d band extends in the FM case down to the VBM of the majority spin, in other words the half-metallic character. Nonetheless it indicates a small density-of-states region just above the majority-spin VBM. The majority spin shows a more distinct two-peak shape below the VBM than in the AFM cases. It also shows a smaller gap for AFM-1 than AFM-2. The overall positions of the peak in the AFM-2 occupied PDOS agree well with the photoemission data of Bhobe *et al.* [13] indicating first a Cr-d-like peak at about 1 eV below the VBM and then N-p-like peaks at about 5 and 7 eV. Further details of the orbital character are provided in the Supplemental Material.

In Fig. 5 we show the band structure for the $[001]_1$ AFM structure. In this case, the relation to the NaCl band structure is easier to recognize as there is only a doubling in the [001] direction (Γ-Z). This structure, however, also clearly has a gap but with a smaller value of about 0.35 eV for the direct gap at Z and 0.24 eV for the indirect gap from X to Z.

Because the QSGW method tends to overestimate gaps, we also calculate the gaps within the 0.8Σ approximation. The values are compared in Table I. In this same table we provide the calculated magnetic moments per Cr atom and the total-energy difference relative to the ground-state AFM-2 phase. The calculations of all phases are performed at the experimental cubic lattice constant of 4.14 Å.

We note that in the 0.8Σ results and in the FM case, the CBM at Γ dips below the VBM at 0.6 Γ-K, so the system becomes semimetallic also for the majority-spin bands. In the AFM-1 case, the gap closes at Z so that system also becomes metallic. The gap in the AFM-2 case persists but is reduced to 0.68 eV (indirect) and 1.04 eV (direct).

For comparison to the experimental data, we also calculated the interband transition optical dielectric function, as
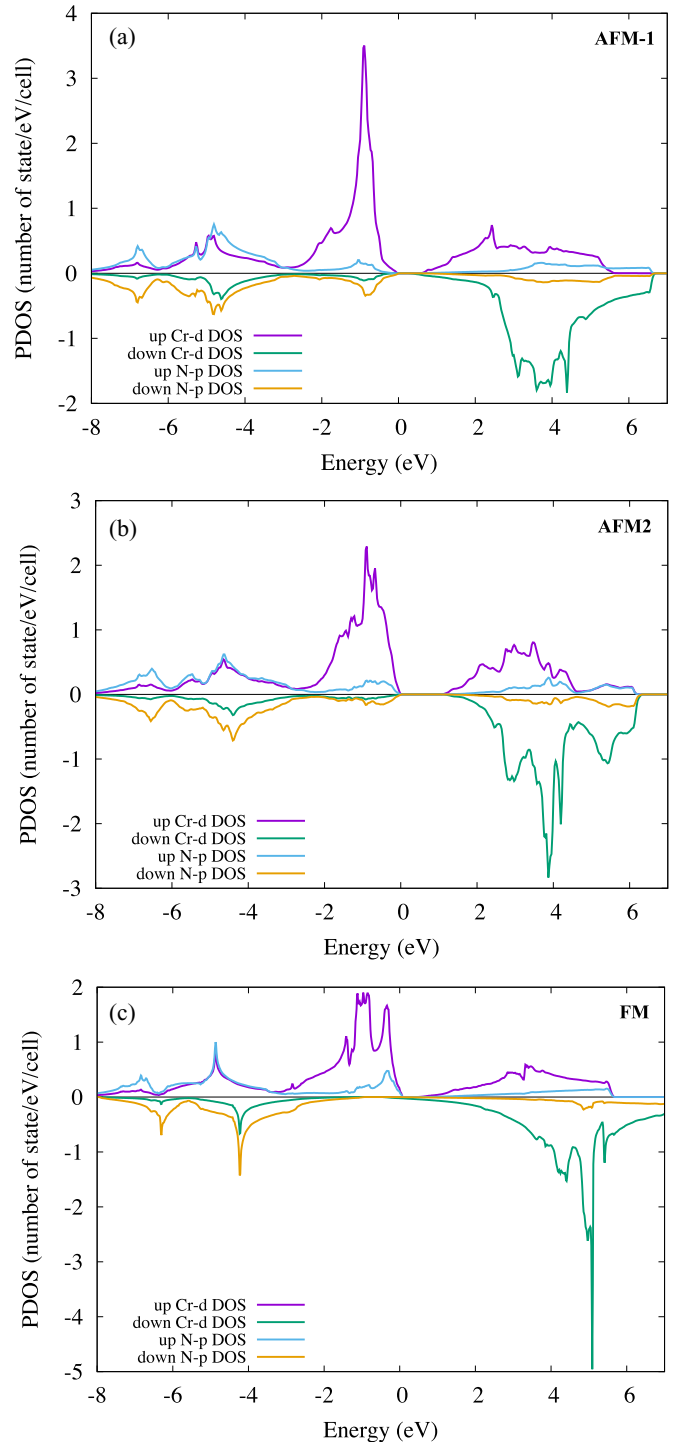

FIG. 4. Partial density of states of Cr-d and N-p in (a) AFM-1 CrN and (b) AFM-2 CrN on one of the Cr atoms and N atoms; (c) FM CrN.

shown in Fig. 6. We put the energy on a logarithmic scale for easier comparison with Fig. 4 in Ref. [14]. We note first that the calculation with and without local-field effects are quite similar, therefore we only show the one including local-field effects. Second, in the experimental results, we left out the low-energy peak below 0.1 eV in the experiment, which according to the analysis by Zhang and Gall [14] corresponds to a vibrational mode. Third, we show our
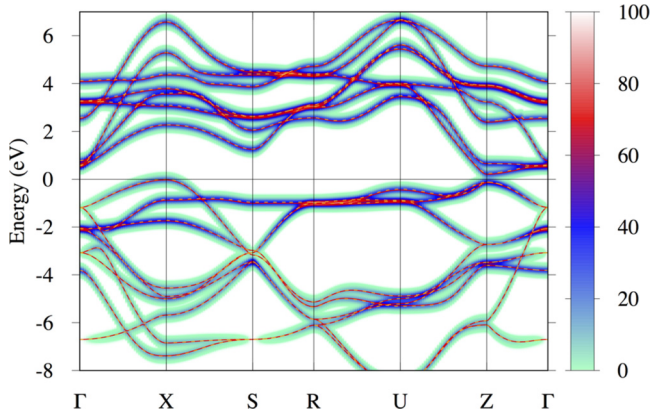
FIG. 5. Band structure of AFM [001]$_1$ CrN with color shading representing the Cr-d contribution.

calculated results using the 0.8Σ approximation. This is done to take into account the underestimate of the screening of W by the neglect of ladder diagrams representing electron-hole coupling in the calculation of the polarization in standard GW. It is found to agree better with experiment than using the full QSGW results. The calculated results are shown for the three phases discussed earlier, the FM, AFM-1 ([001]$_1$), and AFM-2 ([110]$_2$). We can see that for AFM-2, the onset is at the direct gap of 1.0 eV and the first peak in ε_2 is at about 2 eV. This peak somewhat overestimates the experimental peak position in ε_2. The AFM-1 peaks agree somewhat better with the experimental data. The peak in ε_1 agrees reasonably with both AFM1- and AFM-2. In the AFM-1-case, after reducing the $\Delta\Sigma$ by a factor 0.8, the gap has actually closed in a narrow region of the Brillouin zone and hence we see an onset at ~0.5 eV but with a small amplitude or small joint density of states, until about 1 eV, where the absorption increases significantly. From the band structure Fig. 5 we attribute the peak at about 1.5 eV to the set of parallel highest valence and lowest conduction bands along Γ-X. The FM case shows significantly stronger absorption in the region between 0.5
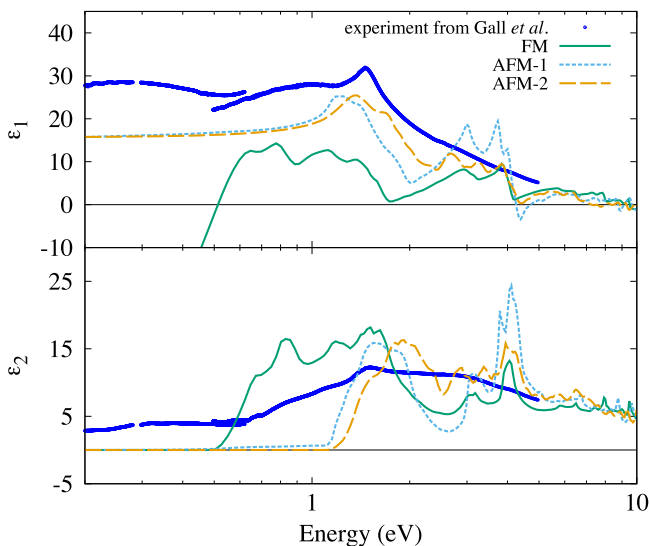

FIG. 6. Optical dielectric function compared with experimental data from Ref. [14].

and 1 eV. This can be attributed to the parallel bands near Γ along Γ-X in Fig. 1 but possibly also to the contribution from intraband transitions in the metallic minority-spin band. The calculation is done at a finite small q and thus does not exclude this intraband contribution. This is responsible for the zero crossing of the ε_1. In a metal, the negative ε_1 at low frequency results from the Drude model, in which $\varepsilon(\omega) = 1 - \omega_P^2/\omega^2$. The free-electron concentration in the minority-spin band electron pocket near X is estimated to be of order 2.4×10^{20} e/cm^3. Assuming an effective mass of 1, this gives a plasmon frequency $\omega_P^2 = 4\pi ne^2/m$ of about $\omega_P = 0.4$ eV which agrees roughly with the zero crossing at about this energy in the calculation. So, this negative region of ε_1 is consistent with a metallic character and the Drude model estimate. The experiment also shows significant absorption in the region 0.6–1.0 eV but no region of negative ε_1. The experimental spectra in this region do not match the ferromagnetic calculated results. So, it should not be taken as evidence of a ferromagnetic phase. Rather it could indicate below gap absorption due to defects, grain boundaries, or surface contributions. We should also keep in mind that the experiment actually corresponds the paramagnetic CrN, which is more difficult to simulate because of the randomness of the spins. It appears though that the experiment captures some optical features similar to those seen in both the AFM-1, AFM-2 ε_2, which we here use as a proxy for the paramagnetic phase. Our calculations would predict a shift of the optical-absorption onset to a larger energy when cooling below the T_N of the AFM-2 structure.

IV. DISCUSSION

The large gap found in the AFM orthorhombic structure in the present QSGW calculation is surprising given the predominant experimental indications in previous work of an optical gap of only 0.64 eV and an even smaller indirect gap of only ~70 meV extracted from transport. Nonetheless, it should be remembered that this corresponded to the paramagnetic state as these works found actually metallic behavior below T_N. On the other hand, Botana et al. [29] ascribed this metallic interpretation to surface states. Our results are more compatible with the hybrid functional calculations of Botana et al. [28] who found a gap as large as 2.13 eV in the AFM state when using the PBE0 hybrid functional with $\alpha = 0.25$ mixing of exact exchange. This is likely an overestimate. Their Yukawa potential PBE0 corresponds to a screened exchange within muffin-tin spheres and comes closest to our full QSGW results with a gap of 1.45 eV compared to our 1.34 eV. Finally, Botana et al.'s TB-mBJ gaps of 0.79, 0.22, and 0 eV in AFM-2, AFM-1, and FM are only slightly larger than our 0.8Σ QSGW result.

Our results thus seem to support Botana et al.'s qualitative conclusions of a significant gap of order 1 eV in the AFM orthorhombic state. Clearly it would be important to find an experimental confirmation of the intrinsic band structure, in a way which avoids perturbing effects from either surface states or N vacancies.

Although QSGW calculations are parameter free, the method of course, still has approximations. In particular, it is known that it tends to overestimate the band gaps in

standard tetrahedral semiconductors by about 20%. This is due primarily to the underestimate of screening inherent in the random-phase approximation (RPA) for calculating W using the polarization $\Pi^0 = iGG$, which neglects electron-hole ladder diagrams. Our results for the optical functions indicate a somewhat better agreement with the optical data after a 0.8Σ correction factor is used.

Additional effects to consider are electron-phonon coupling corrections. However, these are mostly large only in either materials with only low Z elements or in strongly ionic materials with a large LO-TO phonon coupling. Neither is the case here because the band gap occurs between Cr-d states and the almost metallic behavior indicates weak LO-TO splitting, and strong screening of any such lattice-polarization effects.

We thus arrive at the conclusion that the relatively large gap of about 1 eV is really reflective of the underlying intrinsic band structure of AFM CrN indicating indeed a strongly correlated material. The experimental indications of a lower gap or even metallic behavior may thus be largely extrinsic and due to various types of defects, including N vacancies, surfaces, grain boundaries, and so on.

V. CONCLUSIONS

QSGW calculations were carried out for CrN in the low-temperature observed AFM-2 $[110]_2$ phase as well as the hypothetical AFM-1 $[001]_1$ and FM phases. They show a half-metallic FM state and a gap of $\sim$1 eV for the AFM-2 phase and a somewhat lower gap in the AFM-1 phase. These gaps are slightly reduced if we use a 0.8Σ correction for electron-hole effects on the screening. Comparison of the calculated optical dielectric functions with experiment indicate that the 0.8Σ approximation is more accurate. These results differ from recent experimental conclusions asserting a metallic state in the AFM-2 phase. However, they qualitatively agree with other calculations based on hybrid functionals and thereby give additional support to the hypothesis that the observed metallic character below T_N is due to extrinsic factors, such as surface states or N vacancies.

[1] L. M. Corliss, N. Elliott, and J. M. Hastings, Phys. Rev. **117**, 929 (1960).

[2] A. Herwadkar and W. R. L. Lambrecht, Phys. Rev. B **79**, 035125 (2009).

[3] S. Wang, X. Yu, J. Zhang, M. Chen, J. Zhu, L. Wang, D. He, Z. Lin, R. Zhang, K. Leinenweber, and Y. Zhao, Phys. Rev. B **86**, 064111 (2012).

[4] P. S. Herle, M. Hegde, N. Vasathacharya, S. Philip, M. R. Rao, and T. Sripathi, J. Solid State Chem. **134**, 120 (1997).

[5] C. X. Quintela, F. Rivadulla, and J. Rivas, Phys. Rev. B **82**, 245201 (2010).

[6] P. A. Anderson, R. J. Kinsey, S. M. Durbin, A. Markwitz, V. J. Kennedy, A. Asadov, W. Gao, and R. J. Reeves, J. Appl. Phys. **98**, 043903 (2005).

[7] C. Constantin, M. B. Haider, D. Ingram, and A. R. Smith, Appl. Phys. Lett. **85**, 6371 (2004).

[8] D. Gall, C.-S. Shin, R. T. Haasch, I. Petrov, and J. E. Greene, J. Appl. Phys. **91**, 5882 (2002).

[9] X. Y. Zhang, J. S. Chawla, R. P. Deng, and D. Gall, Phys. Rev. B **84**, 073101 (2011).

[10] X. Y. Zhang, J. S. Chawla, B. M. Howe, and D. Gall, Phys. Rev. B **83**, 165205 (2011).

[11] J. R. Frederick and D. Gall, J. Appl. Phys. **98**, 054906 (2005).

[12] J. Frederick, J. D'Arcy-Gall, and D. Gall, Thin Solid Films **494**, 330 (2006).

[13] P. A. Bhobe, A. Chainani, M. Taguchi, T. Takeuchi, R. Eguchi, M. Matsunami, K. Ishizaka, Y. Takata, M. Oura, Y. Senba, H. Ohashi, Y. Nishino, M. Yabashi, K. Tamasaku, T. Ishikawa, K. Takenaka, H. Takagi, and S. Shin, Phys. Rev. Lett. **104**, 236404 (2010).

[14] X. Y. Zhang and D. Gall, Phys. Rev. B **82**, 045116 (2010).

[15] J. Ebad-Allah, B. Kugelmann, F. Rivadulla, and C. A. Kuntscher, Phys. Rev. B **94**, 195118 (2016).

[16] B. Alling, T. Marten, and I. A. Abrikosov, Phys. Rev. B **82**, 184430 (2010).

[17] G. Trimarchi, Z. Wang, and A. Zunger, Phys. Rev. B **97**, 035107 (2018).

[18] J. Varignon, M. Bibes, and A. Zunger, Phys. Rev. B **100**, 035119 (2019).

[19] J. Varignon, M. Bibes, and A. Zunger, Nat. Commun. **10**, 1658 (2019).

[20] F. Rivadulla, M. Bañobre López, C. X. Quintela, A. Piñ eiro, V. Pardo, D. Baldomir, M. A. López-Quintela, J. Rivas, C. A. Ramos, H. Salva, J.-S. Zhou, and J. B. Goodenough, Nat. Mater. **8**, 947 (2009).

[21] A. Filippetti, W. E. Pickett, and B. M. Klein, Phys. Rev. B **59**, 7043 (1999).

[22] A. Filippetti and N. A. Hill, Phys. Rev. Lett. **85**, 5166 (2000).

[23] P. Steneteg, B. Alling, and I. A. Abrikosov, Phys. Rev. B **85**, 144404 (2012).

[24] N. Shulumba, B. Alling, O. Hellman, E. Mozafari, P. Steneteg, M. Odén, and I. A. Abrikosov, Phys. Rev. B **89**, 174108 (2014).

[25] L. Zhou, F. Körmann, D. Holec, M. Bartosik, B. Grabowski, J. Neugebauer, and P. H. Mayrhofer, Phys. Rev. B **90**, 184102 (2014).

[26] A. Lindmaa, R. Lizárraga, E. Holmström, I. A. Abrikosov, and B. Alling, Phys. Rev. B **88**, 054414 (2013).

[27] X. F. Duan, W. B. Mi, Z. B. Guo, and H. L. Bai, J. Appl. Phys. **113**, 023701 (2013).

[28] A. S. Botana, F. Tran, V. Pardo, D. Baldomir, and P. Blaha, Phys. Rev. B **85**, 235118 (2012).

[29] A. S. Botana, V. Pardo, D. Baldomir, and P. Blaha, Phys. Rev. B **87**, 075114 (2013).

[30] Z. Zhang, H. Li, R. Daniel, C. Mitterer, and G. Dehm, Phys. Rev. B **87**, 014104 (2013).

[31] E. Mozafari, B. Alling, P. Steneteg, and I. A. Abrikosov, Phys. Rev. B **91**, 094101 (2015).

[32] T. Rojas and S. E. Ulloa, Phys. Rev. B **96**, 125203 (2017).

[33] T. Rojas and S. E. Ulloa, Phys. Rev. B **98**, 214111 (2018).

[34] M. van Schilfgaarde, T. Kotani, and S. Faleev, Phys. Rev. Lett. **96**, 226402 (2006).

[35] T. Kotani, M. van Schilfgaarde, and S. V. Faleev, Phys. Rev. B **76**, 165106 (2007).

[36] P. Hohenberg and W. Kohn, Phys. Rev. **136**, B864 (1964).

[37] W. Kohn and L. J. Sham, Phys. Rev. **140**, A1133 (1965).

[38] U. von Barth and L. Hedin, J. Phys. C: Solid State Phys. **5**, 1629 (1972).

[39] M. Methfessel, M. van Schilfgaarde, and R. A. Casali, in *Electronic Structure and Physical Properties of Solids. The Use of the LMTO Method*, Lecture Notes in Physics Vol. 535, edited by H. Dreyssé (Springer-Verlag, Berlin, 2000), p. 114.

[40] T. Kotani and M. van Schilfgaarde, Phys. Rev. B **81**, 125117 (2010).

[41] E. Bott, M. Methfessel, W. Krabs, and P. C. Schmidt, J. Math. Phys. **39**, 3393 (1998).

[42] P. E. Blöchl, Phys. Rev. B **50**, 17953 (1994).

[43] V. I. Anisimov, J. Zaanen, and O. K. Andersen, Phys. Rev. B **44**, 943 (1991).

[44] A. I. Liechtenstein, V. I. Anisimov, and J. Zaanen, Phys. Rev. B **52**, R5467 (1995).

[45] L. Hedin, Phys. Rev. **139**, A796 (1965).

[46] L. Hedin and S. Lundqvist, in *Solid State Physics, Advanced in Research and Applications,* edited by F. Seitz, D. Turnbull, and H. Ehrenreich (Academic, New York, 1969), Vol. 23, pp. 1–181.

[47] A. N. Chantis, M. van Schilfgaarde, and T. Kotani, Phys. Rev. Lett. **96**, 086405 (2006).

[48] D. Deguchi, K. Sato, H. Kino, and T. Kotani, Jpn. J. Appl. Phys. **55**, 051201 (2016).

[49] http://www.questaal.org.

[50] ecalj package at https://github.com/tkotani/ecalj/.

[51] D. Pashov, S. Acharya, W. R. Lambrecht, J. Jackson, K. D. Belashchenko, A. Chantis, F. Jamet, and M. van Schilfgaarde, Comput. Phys. Commun. **249**, 107065 (2019).

[52] See Supplemental Material at http://link.aps.org/supplemental/10.1103/PhysRevB.101.085103 for fully *m*-resolved orbital decomposed bands plots.